The Astrophysical Journal Letters, 915:L30 (8pp), 2021 July 10 https://doi.org/10.3847/2041-8213/ac0dc2


# Zero-metallicity Hypernova Uncovered by an Ultra-metal-poor Star in the Sculptor Dwarf Spheroidal Galaxy*

Ása Skúladóttir[1,2], Stefania Salvadori[1,2], Anish M. Amarsi[3], Eline Tolstoy[4], Michael J. Irwin[5], Vanessa Hill[6], Pascale Jablonka[7,8], Giuseppina Battaglia[9,10], Else Starkenburg[4], Davide Massari[4,11], Amina Helmi[4], and Lorenzo Posti[12]

[1] Dipartimento di Fisica e Astronomia, Universitá degli Studi di Firenze, Via G. Sansone 1, I-50019 Sesto Fiorentino, Italy; asa.skuladottir@unifi.it
[2] INAF/Osservatorio Astrofisico di Arcetri, Largo E. Fermi 5, I-50125 Firenze, Italy
[3] Theoretical Astrophysics, Department of Physics and Astronomy, Uppsala University, Box 516, SE-751 20 Uppsala, Sweden
[4] Kapteyn Astronomical Institute, University of Groningen, P.O. Box 800, 9700AV Groningen, The Netherlands
[5] Institute of Astronomy, Madingley Road, Cambridge CB3 0HA, UK
[6] Laboratoire Lagrange, Université de Nice Sophia Antipolis, CNRS, Observatoire de la Côte d'Azur, CS34229, F-06304 Nice Cedex 4, France
[7] Laboratoire d'astrophysique, Ecole Polytechnique Fédérale de Lausanne (EPFL), Observatoire, CH-1290 Versoix, Switzerland
[8] GEPI, Observatoire de Paris, CNRS, Université de Paris Diderot, F-92195 Meudon, Cedex, France
[9] Instituto de Astrofísica de Canarias, Calle Via Láctea s/n, E-38206 La Laguna, Tenerife, Spain
[10] Universidad de La Laguna. Avda. Astrofísico Fco. Sánchez, La Laguna, Tenerife, Spain
[11] INAF—Osservatorio di Astrofisica e Scienza dello Spazio di Bologna, Via Gobetti 93/3, I-40129 Bologna, Italy
[12] Observatoire astronomique de Strasbourg, Université de Strasbourg, 11 rue de l'Université, F-67000 Strasbourg, France
*Received 2021 June 10; revised 2021 June 21; accepted 2021 June 21; published 2021 July 13*

## Abstract

Although true metal-free "Population III" stars have so far escaped discovery, their nature, and that of their supernovae, is revealed in the chemical products left behind in the next generations of stars. Here we report the detection of an ultra-metal-poor star in the Sculptor dwarf spheroidal galaxy AS0039. With $[Fe/H]_{LTE} = -4.11$, it is the most metal-poor star discovered in any external galaxy thus far. Contrary to the majority of Milky Way stars at this metallicity, AS0039 is clearly not enhanced in carbon, with $[C/Fe]_{LTE} = -0.75$, and $A(C) = +3.60$, making it the lowest detected carbon abundance in any star to date. Furthermore, it lacks $\alpha$-element uniformity, having extremely low $[Mg/Ca]_{NLTE} = -0.60$ and $[Mg/Ti]_{NLTE} = -0.86$, in stark contrast with the near solar ratios observed in C-normal stars within the Milky Way halo. The unique abundance pattern indicates that AS0039 formed out of material that was predominantly enriched by a $\sim 20\,M_{\odot}$ progenitor star with an unusually high explosion energy $E = 10 \times 10^{51}$ erg. Therefore, star AS0039 represents some of the first observational evidence for zero-metallicity hypernovae and provides a unique opportunity to investigate the diverse nature of Population III stars.

*Unified Astronomy Thesaurus concepts:* Hypernovae (775); Sculptor dwarf elliptical galaxy (1436); Chemically peculiar stars (226); Population III stars (1285); Population II stars (1284); Galactic archaeology (2178); Chemically peculiar giant stars (1201)

## 1. Introduction

Great advances have been made in the discovery of ancient extremely metal-poor stars ($[Fe/H] < -3$) over the last decade. Within the Milky Way, there are now more than a dozen known stars with $[Fe/H] < -4.5$ (Norris & Yong 2019). In dwarf spheroidal (dSph) and ultra-faint dwarf (UFD) satellite galaxies, dozens of stars have now been discovered with $[Fe/H] < -3$, with the most metal-poor star reaching $[Fe/H] = -3.92 \pm 0.06$ (Tafelmeyer et al. 2010). Of these, almost half of the most metal-poor stars ($[Fe/H] \lesssim -3.4$) belong to the ancient Sculptor dSph galaxy, which is intrinsically metal-poor, $\langle [Fe/H] \rangle = -1.8$, and is dominated by an old stellar population that is >10 Gyr old (Bettinelli et al. 2019).

Extremely metal-poor stars in the Milky Way and its satellite dwarf galaxies show a dichotomy of abundance patterns, namely carbon-enhanced metal-poor (CEMP-no) stars ($[C/Fe]_{LTE} > +0.7$, $[Ba/Fe]_{LTE} \leqslant 0.0$), and carbon-normal stars ($[C/Fe]_{LTE} \leqslant +0.7$). The fraction of CEMP-no stars increases toward lower metallicity and reaches ~70% at $[Fe/H] < -4$ (Lee et al. 2013; Yoon et al. 2018). The abundance patterns of CEMP-no stars have been successfully reproduced by theoretical yields of individual faint supernovae with low explosion energy, along with mixing and fallback (Iwamoto et al. 2005). These faint supernovae release significant amounts of the lighter elements, such as C, O, and Mg, but little amounts of heavier elements such as Fe. This results in high [C/Fe] ratios in their descendants. Often high values of other light-to-heavier element ratios such as [Mg/Fe] are also seen in CEMP-no stars and their $\alpha$-element abundant ratios are typically non-uniform (Norris et al. 2013).

On the other hand, the C-normal stars show a remarkable uniformity in the abundances of the $\alpha$- and the iron-peak elements. This also holds for the most metal-poor C-normal stars found in the Milky Way halo, below $[Fe/H] < -4.5$ (Caffau et al. 2011; Starkenburg et al. 2018). The uniform abundance pattern indicates that these C-normal stars formed from a well-mixed gas polluted by many supernovae (Cayrel et al. 2004).

Here we report the discovery of an ultra-metal-poor star in the Sculptor dSph galaxy, AS0039. Having both low [C/Fe] and non-uniform $\alpha$-element abundance ratios, this star falls outside of the present dichotomy, thereby indicating a different nucleosynthetic origin.

* Based on observations made with ESO VLT/X-SHOOTER at the La Silla Paranal observatory under program ID 0102.B-0786.

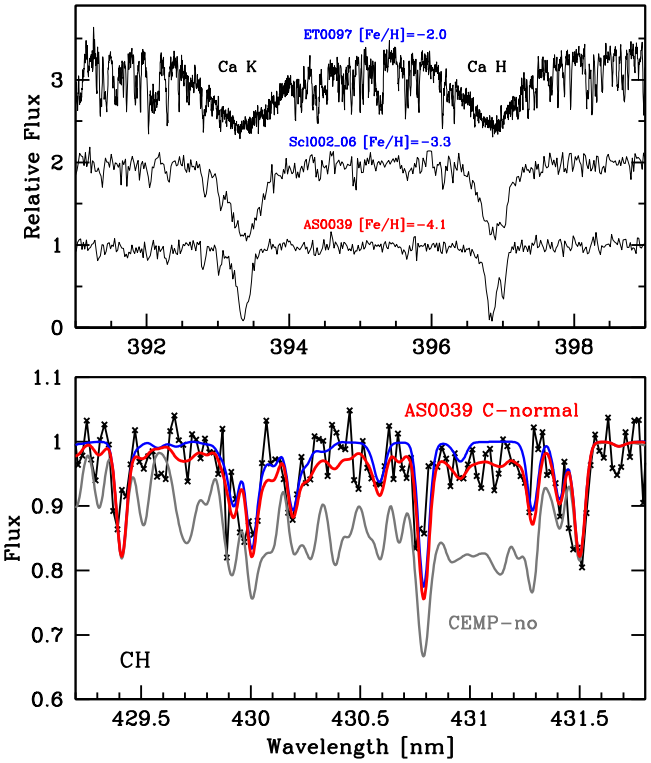


**Figure 1.** Spectrum of AS0039. Top panel: comparison to other metal-poor stars in Sculptor of similar temperature and gravity (Starkenburg et al. 2013; Skúladóttir et al. 2015b). Bottom panel: comparison of the CH G-band region of AS0039 to synthetic spectra: Red shows the best fit, blue is a synthetic spectrum with no CH lines, and gray represents a star born with the minimum amount of [C/Fe] = +0.7 to qualify as a CEMP-no star (accounting for mixing; Placco et al. 2014).

## 2. Observations and Data Reduction

The star AS0039 was a part of a large survey (European Southern Observatory (ESO) ID 0102.B-0786) of the Ca II near-infrared triplet in Sculptor. This low-metallicity star was followed up with the ESO Very Large Telescope (VLT)/X-Shooter for a more detailed abundance analysis. The radial velocity of AS0039 from the X-Shooter spectrum was measured to be $v_{\rm rad} = 135 \pm 1$ km s$^{-1}$. In addition to $v_{\rm rad}$, the star's position, R.A.: 00:58:45.64, decl.:−33:42:24.4; its location on a color–magnitude diagram as, $G = 16.9$, $BP - RP = 1.45$; and its proper motion, $\mu_{\alpha^*} = -0.01 \pm 0.06$ mas yr$^{-1}$, $\mu_\delta = -0.16 \pm 0.05$ mas yr$^{-1}$ (Gaia Collaboration et al. 2021), all confirm AS0039 to be a member of the Sculptor dwarf spheroidal galaxy.

The X-Shooter spectra (see Figure 1) were reduced with the most recent ESO pipeline. The present analysis focuses on the spectra from the UVB ($\lambda = 300$–$560$ nm, $R = 5400$, S/N = 38 pix$^{-1}$ at 468 nm) and the VIS ($\lambda = 550$–$1030$ nm, $R = 8900$, S/N = 42 pix$^{-1}$ at 605 nm) arms. Details of the observations and instrumental set-up are listed in Appendix B.

## 3. Spectral Analysis

### 3.1. Atmospheric Parameters and Stellar Models

The effective temperature, $T_{\rm eff} = 4377 \pm 81$ K, of the star AS0039 was determined from Gaia Early Data Release 3 (eDR3) photometry (Gaia Collaboration et al. 2021; Mucciarelli & Bellazzini 2020). The gravity, $\log g = 0.8 \pm 0.1$, was obtained through photometry, using the known distance to Sculptor (see Skúladóttir et al. 2015b). Finally, the microturbulent velocity, $v_{\rm mic} = 2.0 \pm 0.1$ km s$^{-1}$, was determined with an empirical calibration (Kirby et al. 2009). The best-fitting stellar atmosphere model was taken from MARCS (Gustafsson et al. 2008) and all abundance analyses were carried out using TURBOSPEC (Plez 2012), assuming local thermodynamic equilibrium (LTE), as described in Section 3.2. These LTE abundances were then post-corrected; see Section 3.3.

**Table 1**
Chemical Abundances of AS0039

| Element | $\log\epsilon_\odot$ | [X/Fe]$_{\rm LTE}$ | [X/Fe]$_{\rm NLTE}$ | $\sigma_{\rm NLTE}$ (dex) |
|---|---|---|---|---|
| Fe | 7.46 | −4.11[a] | −3.95[a] | 0.17 |
| C | 8.46 | −0.75 | −0.91 | 0.22 |
| Na | 6.22 | +0.02 | −0.15 | 0.11 |
| Mg | 7.55 | −0.09 | −0.16 | 0.12 |
| Si | 7.51 | +0.06 | −0.15 | 0.28 |
| Ca | 6.30 | +0.65 | +0.44 | 0.11 |
| Sc | 3.14 | −0.24 | −0.40 | 0.28 |
| Ti | 4.97 | +0.66 | +0.70 | 0.13 |
| Cr | 5.62 | +0.04 | +0.58 | 0.18 |
| Sr | 2.83 | −0.91 | −1.07 | 0.22 |
| Li | 0.96 | +3.65[b] | +3.52[b] | ⋯ |
| Al | 6.43 | −1.02[b] | −0.18[b] | ⋯ |
| Mn | 5.42 | −0.76[b] | +0.08[b] | ⋯ |
| Co | 4.94 | +0.07[b] | +0.91[b] | ⋯ |
| Ni | 6.20 | +0.21[b] | +0.21[b] | ⋯ |
| Ba | 2.27 | −1.36[b] | −1.52[b] | ⋯ |

**Notes.**
[a] Results for [Fe/H] are shown.
[b] Upper limits are shown.

### 3.2. LTE Abundances

All measured abundances are listed in Table 1 (see also Appendix A). Not included are the cases where only limits on the level of [X/Fe] > +1 or higher were obtained. The solar abundances were adopted from the recent compilation of Asplund et al. (2021), and all literature data discussed and shown in this Letter has been put on the same scale.

The abundance of C was measured from the CH molecular band at 430 nm. The strength of the CH molecular lines can be affected by the assumed O abundance. Unfortunately, the O I line at 630 nm only gave an upper limit of [O/Fe] < +2. Thus a value of [O/Fe] = +0.6 was assumed for the synthetic spectra, because this corresponds to the average value measured at [Fe/H] < −2 in Sculptor (Hill et al. 2019), and is in good agreement with the Milky Way halo (Amarsi et al. 2019). The best-fitting supernova model (Section 5) implies [O/Fe] ≈ +0.1; nevertheless, a change of Δ[O/Fe] = ±0.5 dex fortunately only had a minor effect, Δ[C/Fe] = ∓0.04 dex, because the C/O ratio stays well below unity in all cases. The N abundance could only be constrained through NH lines to [N/Fe] < +2.20.

The Na abundance was measured from the Na I D resonance lines at 589.0, and 589.6 nm, which gave consistent results within error bars. For the odd elements Al and K, only upper limits could be determined, [Al/Fe] < −1 (Al I 396.2 nm), and [K/Fe] < +1.15 (K I 769.9 nm). The abundance of Sc was measured from two lines of Sc II, at 424.7, and 431.4 nm. The result between those two lines differed by 0.4 dex, which is still consistent given the errors.

The abundances of three $\alpha$-elements were determined: Mg, Ca, and Ti. Four Mg I lines were measured, at 382.9, 383.8,

517.3, and 518.4 nm. The Ca abundance was determined by two Ca I lines (422.7, 616.2 nm), and the near-infrared Ca II triplet. In total, 15 Ti II lines were used for the abundance determination of Ti. A further three Ti I lines were measured, but were ultimately dropped due to large and uncertain non-LTE effects.

With the exception of Cr and Fe, only upper limits for the iron-peak elements could be determined. Four Cr I lines were used for the determination of Cr, while 31 Fe I lines were measured. The upper limits for Mn, Co, and Ni, based on lines of the neutral species, are listed in Table 1, but the upper limits for other elements (V, Cu, Zn) were too high ([X/Fe] $< +1.5$) to be informative.

The only neutron-capture element that could be reliably measured was Sr, which was based on two Sr II lines (407.8, and 421.6 nm) and agreed within error bars. No Ba line was visible in the spectrum, but the Ba II line at 455.4 nm gave the listed upper limit. Other upper limits of neutron-capture elements could not be determined to better than [X/Fe] $< +1$, and in most cases were significantly higher.

The errors were determined as follows. For elements with two or more atomic or ionic lines measured, $N_l \geqslant 2$, the error in $\log N_X/N_H$ was determined as the standard error in the mean. For the remaining elements (C, Si), the error was determined based on the $\chi^2$ of the fits of the synthetic spectra (Skúladóttir et al. 2015a, 2017). The error in the adopted solar abundances (Asplund et al. 2021) were added in quadrature to obtain errors in [X/H]; the error in [Fe/H] was similarly folded into the error estimate for [X/Fe]. Random errors due to the stellar atmospheric parameters were finally folded into these estimates; these were determined to be $\Delta[\mathrm{Fe/H}]_{\mathrm{stellpar}} = 0.16$ dex, and a typical value of $\Delta[\mathrm{X/Fe}]_{\mathrm{stellpar}} = 0.06$ dex was obtained for abundance ratios.

### 3.3. Departure from LTE

The non-LTE corrections for Mg, Ca, and Fe were calculated specifically for this study, using the Balder code (Amarsi et al. 2018; our custom version of Multi3D; Leenaarts & Carlsson 2009). The general method of calculations follows that given in Amarsi et al. (2020); in particular, scattering by background lines, including Rayleigh scattering in the red wing of the Lyman series, was included as described therein. The calculations were performed on 1D spherical MARCS model atmospheres of standard chemical composition, and used recent model atoms (Asplund et al. 2021) that adopt physically motivated descriptions of inelastic collisions with neutral hydrogen. The equivalent widths were determined by direct integration, from which abundance corrections were obtained. These were interpolated onto the stellar parameters $T_{\mathrm{eff}} = 4377$ K and $\log g = 1.0$.

The non-LTE corrections for the other measured elements were generally drawn from the literature: for Na from Lind et al. (2011) via the INSPECT database[13] for Si from Amarsi & Asplund (2017), and for Ti and Cr from Bergemann (2011) and Bergemann & Cescutti (2010) via the NLTE-MPIA database[14] (Kovalev 2019). The corrections for Sc and Sr were neglected for lack of a better alternative; in reality, slightly negative corrections might be expected for these low-excitation, ionized lines. We note that for Sc, rather minor corrections reaching down to $-0.04$ dex have been noted in the literature (Zhang et al. 2014), while for Sr, data in the INSPECT database based on Bergemann et al. (2012) extends down to $\log g = 2.2$, where the mean correction is just $-0.03$ dex.

For the elements with upper limits, only the non-LTE corrections for Li (Barklem et al. 2021; Wang et al. 2021) were drawn from the literature. For Al, Mn, and Co, non-LTE corrections in the literature are large (Nordlander & Lind 2017; Bergemann et al. 2019, 2010), and rather uncertain owing to uncertainties in the atomic data and, in the case of Al, with the equivalent-width method; consequently, a conservative estimate of +1 dex was adopted here. For Ni, the mean abundance correction found for Fe was adopted (+0.16 dex). The correction for the ionized Ba II resonance line was assumed to be negligible by virtue of the extremely low line strength.

Finally, we note that 3D effects are likely to bring the C abundance down (Caffau et al. 2011; Norris & Yong 2019), and Fe slightly up (Amarsi et al. 2016). Consequently, the 3D non-LTE [C/Fe] ratio is expected to be even lower than the 1D value listed in Table 1.

## 4. Results

The spectrum of the newly discovered Sculptor star AS0039 (Figure 1) reveals it to be an ultra-metal-poor star, $[\mathrm{Fe/H}]_{\mathrm{LTE}} = -4.11$ ($[\mathrm{Fe/H}]_{\mathrm{NLTE}} = -3.95$). The low [Fe/H] in combination with extremely low [C/H] and [Mg/H] (Table 1) make AS0039 the most metal-poor star currently known in any external galaxy. The LTE abundance pattern of AS0039 is compared to other Sculptor and Milky Way stars in Figure 2.

While a large fraction (∼70%) of ultra-metal-poor stars (Lee et al. 2013; Yoon et al. 2018) in the Milky Way are carbon-enhanced ([C/Fe] $> +0.7$), this Sculptor star has extremely low $[\mathrm{C/Fe}]_{\mathrm{NLTE}} = -0.91$ (Figure 1). This corresponds to $A(\mathrm{C}) = +3.60$, which is currently the lowest C abundance detected in any galaxy, breaking the recent record, set by the Milky Way star SPLUS J210428.01-004934.2, at $A(\mathrm{C}) = +4.34$ (Placco et al. 2021). The carbon abundance of AS0039 remains low even after correcting for mixing on the upper red giant branch (RGB), which brings processed material to the surface, lowering the C and enhancing the N abundances; following Placco et al. (2014), the initial birth composition becomes $[\mathrm{C/Fe}]_{\mathrm{corr}} = -0.29$. The low C in AS0039 is in line with other stars in Sculptor, which seems to be relatively void of C-rich stars at low metallicities, compared to the Milky Way (Starkenburg et al. 2013; Skúladóttir et al. 2015b).

One of the most notable characteristics of the AS0039 abundance pattern is the low $[\mathrm{Mg/Fe}]_{\mathrm{NLTE}} = -0.16 \pm 0.12$, while C-normal, extremely metal-poor stars in the Milky Way have a tight plateau (Andrievsky et al. 2010) of super-solar $[\mathrm{Mg/Fe}]_{\mathrm{NLTE}} = +0.57 \pm 0.13$. In the rare cases where Mg-poor stars have been discovered, their depletion of Mg is always followed with low abundances of other $\alpha$-elements, such as Ca and Ti. This is not the case for AS0039, where both the [Ca/Fe] and [Ti/Fe] are higher than what is typical for stars at these low metallicities, both in Sculptor and in the Milky Way (Cayrel et al. 2004; Jablonka et al. 2015).

The $\alpha$-element ratios [Mg/Ca] and [Mg/Ti] for AS0039 are compared to the published literature LTE values in Figure 3. The stars of the Milky Way (Cayrel et al. 2004) sit at around $[\mathrm{Mg/Ca}]_{\mathrm{LTE}} = -0.03 \pm 0.10$, which is in sharp contrast with the low value of AS0039, $[\mathrm{Mg/Ca}]_{\mathrm{LTE}} = -0.60 \pm 0.15$. Abundance measurements in other stars in dwarf galaxies, both dSph and UFD, also have a plateau of solar, or even slightly super-solar values of $[\mathrm{Mg/Ca}]_{\mathrm{LTE}}$. Similarly, AS0039 is a clear outlier from

[13] http://www.inspect-stars.com
[14] http://nlte.mpia.de

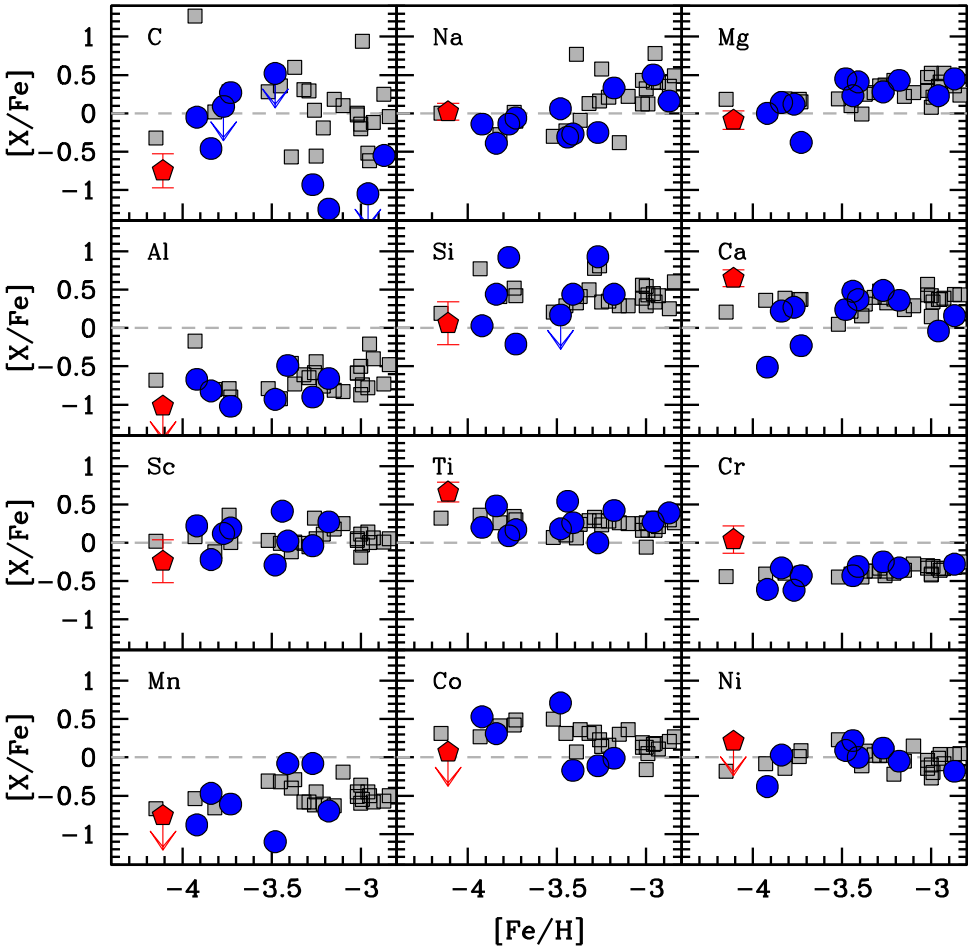


**Figure 2.** Comparison of the LTE abundances of AS0039 (red pentagon) with literature values. Abundances for other Sculptor stars are shown with blue circles (Frebel et al. 2010a; Simon et al. 2010; Tafelmeyer et al. 2010; Starkenburg et al. 2013; Jablonka et al. 2015), while gray squares are stars in the Milky Way (Cayrel et al. 2004).

the normal trend with $[Mg/Ti]_{LTE} = -0.82 \pm 0.16$, while the Milky Way has an average value (Cayrel et al. 2004) of $[Mg/Ti]_{LTE} = +0.08 \pm 0.12$. The ratios of [Mg/Ti] in the Sculptor dSph differ from other galaxies, both the Milky Way and other dwarf galaxies, with a declining trend toward lower [Fe/H]. Combined with the lack of CEMP stars in this galaxy, this is further evidence that the earliest chemical enrichment of Sculptor was significantly different from that of the Milky Way. The lack of known stars in other dwarf galaxies at $[Fe/H] < -3.5$ makes it currently impossible to conclude whether this trend of [Mg/Ti] is unique for Sculptor, or a common trait of dSph, or even UFD galaxies. To ensure a fair comparison, Figure 3 is limited to RGB stars, but we note that the uniformity of $\alpha$-elements in the Milky Way C-normal stars extends down to the lowest $[Fe/H] < -4.5$ (Caffau et al. 2011; Starkenburg et al. 2018).

The extreme $\alpha$-element ratios are not the only distinctive feature in the abundance pattern of AS0039, which also has high $[Cr/Fe]_{NLTE} = +0.58 \pm 0.18$ compared to the tight plateau around the solar ratio that is observed in the metal-poor Milky Way halo (Bergemann & Cescutti 2010), with $[Cr/Fe]_{NLTE} = 0.00 \pm 0.06$. Quite low upper limits were obtained for the odd elements Al, Mn, and Co, comparable to or lower than the typically measured values in Sculptor, while the odd element Na in AS0039 has a normal abundance for extremely metal-poor stars. Finally, the extremely low abundance of the neutron-capture elements, $[Ba/H] \leqslant -5.5$ and $[Sr/H] = -5.02 \pm 0.22$ are typical for pristine second-generation stars (Jablonka et al. 2015).

On the whole, the abundance pattern of AS0039 is starkly different from all other extremely metal-poor stars that have been discovered in the Milky Way or its satellite galaxies. This suggests that AS0039 was not formed from well-mixed material enriched by many supernovae; instead, it is showing a dominant contribution from only one single event. This is in line with theoretical studies that have shown that a single supernovae is sufficient to reach metallicities of $[Fe/H] = -4$ in dwarf galaxies (Cooke & Madau 2014; Rossi et al. 2021). Therefore, AS0039 opens up a new window into the diverse properties of the Population III stars.

## 5. Formation Scenario

To investigate the formation scenario of AS0039, its observed abundances were compared to nucleosynthetic stellar yields of Population III supernovae over a large range of progenitor masses (10–100 $M_{\odot}$), explosion energies ($(0.3–10) \times 10^{51}$ erg), and internal mixing efficiencies (Heger & Woosley 2010), using the Starfit tool.[15] The best fit revealed that the unique abundance pattern of AS0039 shows a dominant signature of a $M = 21\ M_{\odot}$

[15] http://starfit.org

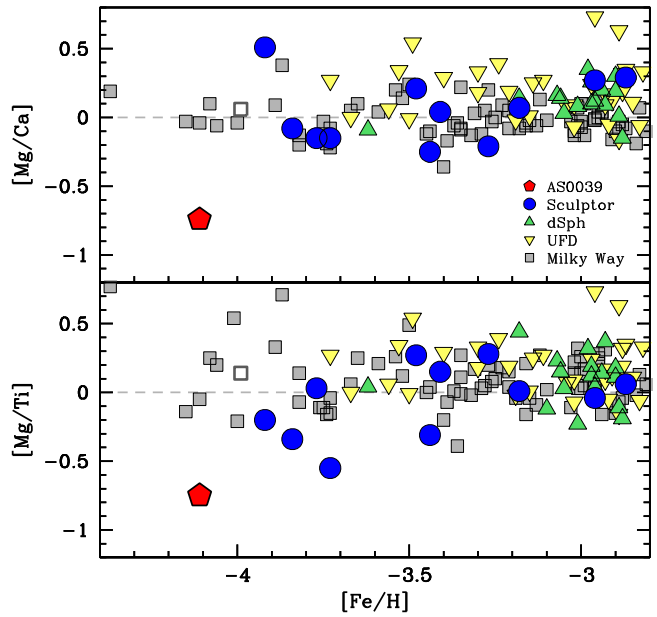


**Figure 3.** Comparison of the 1D LTE $\alpha$-element ratios of AS0039 to those of the literature, [Mg/Ca] (top panel) and [Mg/Ti] (bottom panel). Classical 1D LTE abundances for RGB stars in Sculptor (blue), other dSph galaxies (green), the UFD galaxies (yellow), and C-normal RGB stars in the Milky Way Suda et al. (2008). The Milky Way star SPLUS J210428.01-004934.2 (Placco et al. 2021) is shown with a gray open square.

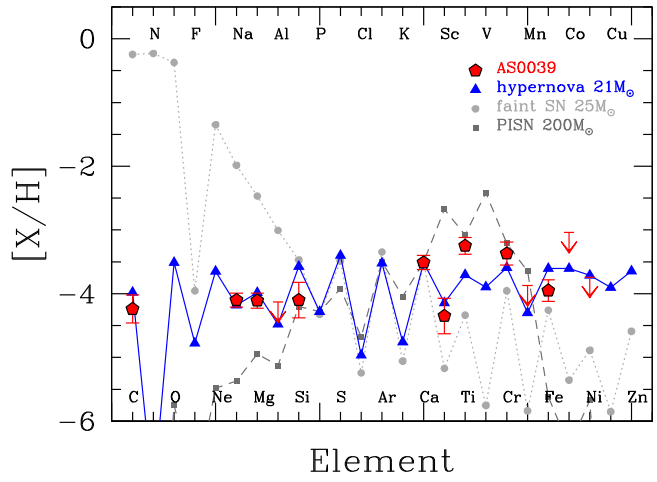


**Figure 4.** Non-LTE abundance pattern of AS0039 (red pentagons) compared to theoretical models. Blue triangles show the best-fitting model of a zero-metallicity 21 $M_\odot$ hypernovae, of energy $10 \times 10^{51}$ erg. Also depicted are models for a Population III faint supernova of 25 $M_\odot$ with $E = 0.7 \times 10^{51}$ erg (light gray circles), and pair-instability supernova of 200 $M_\odot$ (dark gray squares). All models are normalized to the measured $[Ca/H]_{NLTE}$ of AS0039. The C abundance of AS0039 has been corrected for internal mixing (Placco et al. 2014).

hypernovae, with $E = 10 \times 10^{51}$ erg, see Figure 4. For confirmation, we also used our own fitting routine (Salvadori et al. 2019), which gave the best fit of a hypernovae with $M = 20 \pm 2$ $M_\odot$, in good agreement with the result obtained with Starfit.

For comparison, we also show an example of a model of a typical faint supernova (Figure 4), since such models have been very successful in explaining the origin of CEMP-no stars (Iwamoto et al. 2005), and a pair-instability supernovae (PISN) of a typical mass $M = 200$ $M_\odot$. Such PISN enrich their surroundings with large amounts of Fe, and thus their descendants are typically expected at much higher metallicities, $[Fe/H] \approx -2$ (Salvadori et al. 2019). Both faint supernovae and PISN can be excluded as having a dominant contribution to AS0039.

The high explosion energies of hypernovae permit simultaneously low [C/Fe], [Mg/Ca], and [Mg/Ti]. While C and Mg have hydrostatic origin, and are mainly created in fusion throughout the lifetime of the star, both Ca and Ti are so-called explosive $\alpha$-elements that mainly form in the supernova itself. With the higher explosion energy of the hypernovae, relatively high amounts of Ca and Ti are formed, resulting in a low [Mg/Ca, Ti] ratio, as is observed in AS0039. The opposite is true in faint supernova, and close to half of CEMP-no stars have high [Mg/Ca] $\gtrsim +0.5$ (Norris et al. 2013). During these faint supernova, only the outer C-rich layers are expelled, while the Fe-rich center of the star falls into the black hole, resulting in very high [C/Fe] ratios (Iwamoto et al. 2005). We note that none of the available models (Heger & Woosley 2010) were able to reproduce the high [Ti/Fe] observed in AS0039. However, this is in line with other results, where theoretical models are known to systematically under-produce Ti relative to observations at all metallicities (Heger & Woosley 2010; Kobayashi et al. 2020).

## 6. Discussion

With a striking signature of simultaneously low values of [C/Fe] and [Mg/Ca,Ti], the star AS0039 is the first unambiguous evidence of a hypernova imprint in any of the Milky Way satellite galaxies. In the Milky Way halo, there are two other possible detections reported in the literature, although each display rather different abundance signatures. We discuss these in turn below.

Recently it was argued that the CEMP-no star HE 1327−2326 in the Milky Way halo shows an imprint of a supernova with rather high explosion energy, $E = 5 \times 10^{51}$ erg (Ezzeddine et al. 2019). However, their models depend on asymmetrical effects, which are still poorly understood; moreover, these effects introduce three additional free parameters to be fitted. Furthermore, more recent models struggle to produce the large [C/Fe] observed in HE 1327−2326 (Grimmett et al. 2021). In contrast, the abundance pattern of AS0039 can be matched by a simple spherical hypernova, without having to invoke any additional physics and free parameters.

Even more recently, Placco et al. (2021) presented results for SPLUS J210428.01-004934.2. They demonstrated that its abundance pattern is best fit with a progenitor of 30 $M_\odot$, that is ∼50% larger than that of AS0039, but with the same explosion energy ($E = 10 \times 10^{51}$ erg). Interestingly, although J210428.01-004934.2 is also somewhat low in C, $[C/Fe]_{LTE} = -0.1$, it displays $[Mg/Ca,Ti]_{LTE}$ ratios that are close to zero, in stark contrast to the atypically low values measured in AS0039 (Figure 3). Clearly the abundance signatures of Population III hypernovae have a strong mass dependence, and further observations are needed to fully understand the diversity of the first generations of stars.

## 7. Conclusion

New ESO VLT/X-Shooter observations have revealed that at $[Fe/H]_{LTE} = -4.11$ ($[Fe/H]_{NLTE} = -3.95$), with unusually low $[Mg/Fe]_{NLTE} = -0.16$, and $[C/Fe]_{corr} = -0.29$, the star AS0039 in the Sculptor dwarf spheroidal is the most metal-poor star that has been discovered in an external galaxy. Furthermore, it has the currently lowest detected C abundance, $A(C) = +3.60$, in any

galaxy. In addition to the overall low metallicity, this star has a unique abundance pattern, with particularly low ratios of hydrostatic-to-explosive $\alpha$-elements ([Mg/Ca,Ti] $< -0.6$). The detailed non-LTE abundance pattern of AS0039 can best be explained with a Population III progenitor of $M = 21\,M_{\odot}$, and high explosion energy $E = 10 \times 10^{51}$ erg, making AS0039 one of the first observational evidence of a zero-metallicity hypernova.

The number of known stars in the Milky Way, at [Fe/H] $< -3.5$, is almost an order of magnitude higher than in the dwarf galaxy satellites (Suda et al. 2008). Given the available data, it is unlikely merely a coincidence that one of two known first descendants of a zero-metallicity hypernova is found in Sculptor. First of all, the galaxy formed as much as 80% of its stars 12–14 Gyr ago (Bettinelli et al. 2019), and thus it gives an unobscured view to the earliest star formation. Second, Sculptor may lie in a sweet spot in terms of mass. Compared to UFD galaxies it is relatively massive (Battaglia et al. 2008), with $M_{\rm tot} \gtrsim 4 \times 10^8$. If a rare event such as a hypernova were to occur in a much smaller UFD galaxy, it would likely be too small to retain the yields of such an energetic event (Cooke & Madau 2014). At the same time, given the modest size and star formation rate of Sculptor, the imprints of hypernovae will not be lost or rapidly diluted by subsequent star formation events. Consequently, Sculptor dwarf spheroidal galaxy may be the ideal system for further discoveries.

Until now, the observational evidence for Population III stars has been completely dominated by the imprints of faint supernovae seen in CEMP-no stars. However, these low-energy supernovae only occupy a limited portion of the parameter space that has been theoretically predicted for Population III stars. With the discovery of AS0039, we are expanding this view for the first time, opening a window into the investigation of the most energetic primordial supernovae, i.e., Population III hypernovae. Combined with advances in theoretical simulations of early galaxy formation and improved data from upcoming large spectroscopic surveys (e.g., Christlieb et al. 2019), this discovery will enable us to assemble the full picture of the elusive nature of the first stars in the universe.

These results are based on VLT/FLAMES and VLT/X-Shooter observations collected at the European Organisation for Astronomical Research (ESO) in the Southern Hemisphere under program ESO ID 0102.B-0786. This project has received funding from the European Research Council (ERC) under the European Union's Horizon 2020 research and innovation program (grant agreement No. 804240). A.M.A. gratefully acknowledges support from the Swedish Research Council (VR 2020-03940). G.B. acknowledges financial support through the grant (AEI/FEDER, UE) AYA2017-89076-P, as well as by the Ministerio de Ciencia, Innovación y Universidades (MCIU), through the State Budget and by the Consejería de Economía, Industria, Comercio y Conocimiento of the Canary Islands Autonomous Community, through the Regional Budget. E.S. acknowledges funding through VIDI grant "Pushing Galactic Archaeology to its limits" (with project number VI.Vidi.193.093) which is funded by the Dutch Research Council (NWO). This work was supported by computational resources provided by the Australian Government through the National Computational Infrastructure (NCI) under the National Computational Merit Allocation Scheme (NCMAS) and Australian National University Merit Allocation Scheme (ANUMAS).

*Facilities:* ESO VLT/FLAMES, ESO VLT/X-SHOOTER, Gaia.

## Appendix A
## Literature Compilation

The measured abundance ratios of [Mg/Ca] and [Mg/Ti] in AS0039 are compared to literature values in Figure 3. Typically, only LTE abundance analysis is provided in the literature (Suda et al. 2008). However, non-LTE effects for similar stars (in terms of $T_{\rm eff}$, log $g$, and [Fe/H]) are expected to be in the same direction and have comparable magnitudes. All existing stellar abundance measurements in dwarf galaxies are for RGB stars, as main-sequence stars are too faint for such analysis to be feasible. Therefore, in Figure 3 we only include RGB stars in the Milky Way to ensure a fair comparison. Where provided, literature abundances based on Fe I and Ti II are chosen, to be as consistent to the analysis of AS0039 as possible.

To show the uniqueness of [Mg/Ca] and [Mg/Ti] in AS0039, our literature compilation was quite extensive, especially in relation to other dwarf galaxies. Figure 3 includes classical 1D LTE abundances for RGB stars in Sculptor (Frebel et al. 2010a; Tafelmeyer et al. 2010; Starkenburg et al. 2013; Jablonka et al. 2015; Simon et al. 2015), other dSph galaxies (Shetrone et al. 2001; Cohen & Huang 2009, 2010; Tafelmeyer et al. 2010; Kirby & Cohen 2012; Theler et al. 2020), the UFD galaxies (Chiti et al. 2018; François et al. 2016; Frebel et al. 2010b, 2014, 2016; Norris et al. 2010b; Gilmore et al. 2013; Ji et al. 2016a, 2016b, 2016c, 2019; Norris et al. 2010a; Roederer & Kirby 2014; Simon et al. 2010; Venn et al. 2017), and C-normal RGB stars in the Milky Way (Cayrel et al. 2004; Lai et al. 2008; Yong et al. 2013; Roederer et al. 2014). All literature data shown or discussed in this Letter have been put to the same solar abundance scale (Asplund et al. 2021).

The general abundance pattern of AS0039, compared to other Sculptor stars, and the Milky Way, is shown in Figure 2.

## Appendix B
## Additional Tables

Detailed information about the star AS0039 and the X-Shooter spectra used in this analysis are listed in Table 2. A list of the Fe lines used for the abundance analysis is given in Table 3, and information for other elemental lines are in Table 4.

**Table 2**
Observational Log for the X-Shooter Spectra of AS0039

| Star | AS0039 |
|---|---|
| R.A. | 00:58:45.64 |
| Decl. | −33:42:24.4 |
| Obs. date | 2018-12-16 |
| Exp. time | 2 × 1800s |
| Airmass (mean) | 1.1 |
| Seeing (mean) | 0.″6 |
| Slit width (UVB) | 1.″0 |
| $R_{\rm UVB}$ | 5 400 |
| $\lambda_{\rm UVB}$ | 3000–5600 Å |
| $S/N_{\rm UVB}$ (4680 Å) | 38 pxl$^{-1}$ |
| Slit width (VIS) | 0.″9 |
| $R_{\rm VIS}$ | 8 900 |
| $\lambda_{\rm VIS}$ | 5500–10200 Å |
| $S/N_{\rm VIS}$ (6050 Å) | 42 pxl$^{-1}$ |

**Table 2**
(Continued)

| Star | AS0039 |
|---|---|
| G | $16.932 \pm 0.001$ |
| BP | $17.525 \pm 0.010$ |
| RP | $16.073 \pm 0.010$ |
| $\mu_{\alpha^*}$ | $-0.01 \pm 0.06$ mas yr$^{-1}$ |
| $\mu_\delta$ | $-0.16 \pm 0.05$ mas yr$^{-1}$ |
| $v_{\rm rad}$ | $135 \pm 1$ km s$^{-1}$ |
| $T_{\rm eff}$ | $4377 \pm 81$ K |
| log $g$ | $0.8 \pm 0.1$ |
| $v_{\rm mic}$ | $2.0 \pm 0.1$ km s$^{-1}$ |

**Table 3**
Measurements of Individual Fe Lines

| Species | $\lambda$/nm | $\chi_{\rm low}$ | log$gf$ | log$\epsilon_{\rm LTE}$ | $\Delta_{\rm NLTE}$ (dex) |
|---|---|---|---|---|---|
| Fe I | 381.584 | 1.490 | 0.237 | 3.37 | 0.17 |
| Fe I | 381.634 | 2.200 | −1.196 | | |
| Fe I | 382.043 | 0.860 | 0.119 | 3.21 | 0.19 |
| Fe I | 382.118 | 3.270 | 0.198 | | |
| Fe I | 382.430 | 3.300 | −0.043 | 3.38 | 0.18 |
| Fe I | 382.444 | 0.000 | −1.362 | | |
| Fe I | 382.588 | 0.920 | −0.037 | 2.81 | 0.21 |
| Fe I | 382.782 | 1.560 | 0.062 | 2.70 | 0.24 |
| Fe I | 385.082 | 0.990 | −1.734 | 3.00 | 0.17 |
| Fe I | 386.552 | 1.010 | −0.982 | 3.75 | 0.07 |
| Fe I | 387.250 | 0.990 | −0.928 | 3.47 | 0.12 |
| Fe I | 389.789 | 2.690 | −0.736 | 3.40 | 0.18 |
| Fe I | 389.801 | 1.010 | −2.018 | | |
| Fe I | 390.648 | 0.110 | −2.243 | 2.79 | 0.22 |
| Fe I | 392.026 | 0.120 | −1.746 | 3.16 | 0.18 |
| Fe I | 392.291 | 0.050 | −1.651 | 3.91 | 0.09 |
| Fe I | 400.524 | 1.560 | −0.610 | 3.80 | 0.06 |
| Fe I | 404.581 | 1.490 | 0.280 | 2.83 | 0.20 |
| Fe I | 406.359 | 1.560 | 0.062 | 3.57 | 0.09 |
| Fe I | 407.174 | 1.610 | −0.022 | 3.43 | 0.11 |
| Fe I | 413.206 | 1.610 | −0.675 | 3.79 | 0.06 |
| Fe I | 414.342 | 3.050 | −0.204 | 3.63 | 0.18 |
| Fe I | 414.387 | 1.560 | −0.511 | | |
| Fe I | 419.825 | 3.370 | −0.457 | 3.64 | 0.20 |
| Fe I | 419.830 | 2.400 | −0.719 | | |
| Fe I | 420.203 | 1.490 | −0.708 | 3.53 | 0.10 |
| Fe I | 423.594 | 2.420 | −0.341 | 3.20 | 0.24 |
| Fe I | 425.012 | 2.470 | −0.405 | 3.80 | 0.19 |
| Fe I | 425.079 | 1.560 | −0.714 | 3.44 | 0.11 |
| Fe I | 426.047 | 2.400 | 0.109 | 3.56 | 0.20 |
| Fe I | 432.576 | 1.610 | 0.006 | 3.32 | 0.13 |
| Fe I | 438.355 | 1.490 | 0.200 | 3.05 | 0.17 |
| Fe I | 441.512 | 1.610 | −0.615 | 2.73 | 0.26 |
| Fe I | 442.731 | 0.050 | −2.924 | 3.44 | 0.17 |
| Fe I | 446.165 | 0.090 | −3.210 | 3.37 | 0.18 |
| Fe I | 448.217 | 0.110 | −3.501 | 3.34 | 0.19 |
| Fe I | 448.225 | 2.220 | −1.482 | | |
| Fe I | 452.861 | 2.180 | −0.822 | 3.25 | 0.23 |

**Table 4**
Atomic Data and Measured Abundances of Individual Lines

| Species | $\lambda$/nm | $\chi_{\rm low}$ | log$gf$ | log$\epsilon_{\rm LTE}$ | $\Delta_{\rm NLTE}$ (dex) |
|---|---|---|---|---|---|
| Li I | 670.776 | 0.000 | −0.002 | 0.50[a] | 0.03 |
| Li I | 670.792 | 0.000 | −0.303 | | |
| Na I | 588.995 | 0.000 | 0.117 | 2.24 | −0.06 |
| Na I | 589.592 | 0.000 | −0.194 | 2.01 | 0.06 |
| Mg I | 382.936 | 2.709 | −0.231 | 3.59 | 0.06 |
| Mg I | 383.829 | 2.717 | −1.530 | 3.20 | 0.12 |
| Mg I | 383.829 | 2.717 | 0.392 | | |
| Mg I | 383.830 | 2.717 | −0.355 | | |
| Mg I | 517.268 | 2.712 | −0.402 | 3.26 | 0.11 |
| Mg I | 518.360 | 2.717 | −0.180 | 3.35 | 0.07 |
| Al I | 396.152 | 0.014 | −0.323 | 1.30[a] | 1.00 |
| Si I | 390.552 | 1.909 | −1.041 | 3.46 | −0.05 |
| Ca I | 422.673 | 0.000 | 0.244 | 2.59 | 0.07 |
| Ca I | 616.217 | 1.899 | −0.090 | 2.82 | 0.15 |
| Ca II | 849.802 | 1.692 | −1.416 | 3.01 | −0.28 |
| Ca II | 854.209 | 1.700 | −0.463 | 2.82 | −0.07 |
| Ca II | 866.214 | 1.692 | −0.723 | 2.94 | −0.09 |
| Sc II | 424.682 | 0.315 | 0.242 | −1.47 | 0.00 |
| Sc II | 431.408 | 0.618 | −0.096 | −0.95 | 0.00 |
| Ti I | 441.727 | 1.887 | −0.020 | 1.64[b] | 0.16 |
| Ti I | 447.124 | 1.734 | −0.103 | 2.17[b] | 0.16 |
| Ti I | 501.419 | 0.000 | −1.220 | 1.43[b] | 0.57 |
| Ti I | 501.428 | 0.813 | 0.110 | | |
| Ti II | 390.054 | 1.131 | −0.200 | 1.51 | 0.36 |
| Ti II | 391.346 | 1.116 | −0.420 | 1.43 | 0.34 |
| Ti II | 428.787 | 1.080 | −1.790 | 1.74 | 0.17 |
| Ti II | 430.004 | 1.180 | −0.440 | 1.38 | 0.33 |
| Ti II | 430.191 | 1.161 | −1.150 | 1.62 | 0.24 |
| Ti II | 431.497 | 1.161 | −1.100 | 2.04 | 0.25 |
| Ti II | 433.791 | 1.080 | −0.960 | 1.44 | 0.19 |
| Ti II | 439.503 | 1.084 | −0.540 | 1.58 | 0.24 |
| Ti II | 439.977 | 1.237 | −1.190 | 1.73 | 0.26 |
| Ti II | 444.379 | 1.080 | −0.720 | 1.09 | 0.02 |
| Ti II | 445.048 | 1.084 | −1.520 | 1.83 | 0.17 |
| Ti II | 446.851 | 1.131 | −0.600 | 1.37 | 0.02 |
| Ti II | 450.127 | 1.116 | −0.770 | 1.26 | 0.24 |
| Ti II | 457.197 | 1.572 | −0.320 | 1.07 | 0.12 |
| Ti II | 518.868 | 1.582 | −1.050 | 1.68 | 0.15 |
| Cr I | 428.972 | 0.000 | −0.361 | 1.35 | 0.89 |
| Cr I | 520.451 | 0.940 | −0.208 | 1.90 | 0.64 |
| Cr I | 520.604 | 0.940 | 0.019 | 1.77 | 0.65 |
| Cr I | 520.843 | 0.940 | 0.158 | 1.17 | 0.66 |
| Mn I | 403.075 | 0.000 | −0.470 | 0.70[a] | 1.00 |
| Mn I | 403.306 | 0.000 | −0.618 | 0.40[a] | 1.00 |
| Co I | 399.530 | 0.923 | −0.220 | 0.90[a] | 1.00 |
| Ni I | 547.690 | 1.826 | −0.890 | 2.30[a] | 0.16 |
| Sr II | 407.771 | 0.000 | 0.167 | −2.00 | 0.00 |
| Sr II | 421.552 | 0.000 | −0.145 | −2.38 | 0.00 |
| Ba II | 455.403 | 0.000 | 0.170 | −3.20[a] | 0.00 |

**Notes.**
[a] Upper limits are shown.
[b] Ti I excluded from the mean.

## ORCID iDs

Ása Skúladóttir https://orcid.org/0000-0001-9155-9018
Stefania Salvadori https://orcid.org/0000-0001-7298-2478
Anish M. Amarsi https://orcid.org/0000-0002-3181-3413
Eline Tolstoy https://orcid.org/0000-0002-3047-4843
Michael J. Irwin https://orcid.org/0000-0002-2191-9038

Pascale Jablonka https://orcid.org/0000-0002-9655-1063
Giuseppina Battaglia https://orcid.org/0000-0002-6551-4294
Else Starkenburg https://orcid.org/0000-0003-4501-103X
Davide Massari https://orcid.org/0000-0001-8892-4301
Amina Helmi https://orcid.org/0000-0003-3937-7641
Lorenzo Posti https://orcid.org/0000-0001-9072-5213

## References

Amarsi, A. M., & Asplund, M. 2017, MNRAS, 464, 264
Amarsi, A. M., Lind, K., Asplund, M., Barklem, P. S., & Collet, R. 2016, MNRAS, 463, 1518
Amarsi, A. M., Lind, K., Osorio, Y., et al. 2020, A&A, 642, A62
Amarsi, A. M., Nissen, P. E., & Skúladóttir, Á. 2019, A&A, 630, A104
Amarsi, A. M., Nordlander, T., Barklem, P. S., et al. 2018, A&A, 615, A139
Andrievsky, S. M., Spite, M., Korotin, S. A., et al. 2010, A&A, 509, A88
Asplund, M., Amarsi, A. M., & Grevesse, N. 2021, arXiv:2105.01661
Barklem, P. S., Amarsi, A. M., Grumer, J., et al. 2021, ApJ, 908, 245
Battaglia, G., Helmi, A., Tolstoy, E., et al. 2008, ApJL, 681, L13
Bergemann, M. 2011, MNRAS, 413, 2184
Bergemann, M., & Cescutti, G. 2010, A&A, 522, A9
Bergemann, M., Gallagher, A. J., Eitner, P., et al. 2019, A&A, 631, A80
Bergemann, M., Hansen, C. J., Bautista, M., & Ruchti, G. 2012, A&A, 546, A90
Bergemann, M., Pickering, J. C., & Gehren, T. 2010, MNRAS, 401, 1334
Bettinelli, M., Hidalgo, S. L., Cassisi, S., et al. 2019, MNRAS, 487, 5862
Caffau, E., Bonifacio, P., François, P., et al. 2011, Natur, 477, 67
Cayrel, R., Depagne, E., Spite, M., et al. 2004, A&A, 416, 1117
Chiti, A., Frebel, A, Ji, A. P, et al. 2018, ApJ, 857, 74
Christlieb, N., Battistini, C., Bonifacio, P., et al. 2019, Msngr, 175, 26
Cohen, J. G., & Huang, W. 2009, ApJ, 701, 1053
Cohen, J. G., & Huang, W. 2010, ApJ, 719, 931
Cooke, R. J., & Madau, P. 2014, ApJ, 791, 116
Ezzeddine, R., Frebel, A., Roederer, I. U., et al. 2019, ApJ, 876, 97
François, P., Monaco, L., Bonifacio, P., et al. 2016, A&A, 588, A7
Frebel, A., Kirby, E. N., & Simon, J. D. 2010a, Natur, 464, 72
Frebel, A., Norris, J. E., Gilmore, G., & Wyse, R. F. G. 2016, ApJ, 826, 110
Frebel, A., Simon, J. D., Geha, M., & Willman, B. 2010b, ApJ, 708, 560
Frebel, A., Simon, J. D., & Kirby, E. N. 2014, ApJ, 786, 74
Gaia Collaboration, Brown, A. G. A., Vallenari, A., et al. 2021, A&A, 649, A1
Gilmore, G., Norris, J. E., Monaco, L., et al. 2013, ApJ, 763, 61
Grimmett, J. J., Müller, B., Heger, A., Banerjee, P., & Obergaulinger, M. 2021, MNRAS, 501, 2764
Gustafsson, B., Edvardsson, B., Eriksson, K., et al. 2008, A&A, 486, 951
Heger, A., & Woosley, S. E. 2010, ApJ, 724, 341
Hill, V., Skúladóttir, Á., Tolstoy, E., et al. 2019, A&A, 626, A15
Iwamoto, N., Umeda, H., Tominaga, N., Nomoto, K., & Maeda, K. 2005, Sci, 309, 451
Jablonka, P., North, P., Mashonkina, L., et al. 2015, A&A, 583, A67
Ji, A. P., Frebel, A., Ezzeddine, R., & Casey, A. R. 2016a, ApJL, 832, L3
Ji, A. P., Frebel, A., Simon, J. D., & Chiti, A. 2016b, ApJ, 830, 93
Ji, A. P., Frebel, A., Simon, J. D., & Geha, M. 2016c, ApJ, 817, 41
Ji, A. P., Simon, J. D., Frebel, A., Venn, K. A., & Hansen, T. T. 2019, ApJ, 870, 83
Kirby, E. N., & Cohen, J. G. 2012, AJ, 144, 168
Kirby, E. N., Guhathakurta, P., Bolte, M., Sneden, C., & Geha, M. C. 2009, ApJ, 705, 328
Kobayashi, C., Karakas, A. I., & Lugaro, M. 2020, ApJ, 900, 179
Kovalev, M. 2019, PhD thesis, Universität Heidelberg
Lai, D. K., Bolte, M., Johnson, J. A., et al. 2008, ApJ, 681, 1524
Lee, Y. S., Beers, T. C., Masseron, T., et al. 2013, AJ, 146, 132
Leenaarts, J., & Carlsson, M. 2009, in ASP Conf. Ser. 415, The Second Hinode Science Meeting: Beyond Discovery-Toward Understanding, ed. B. Lites et al. (San Francisco, CA: ASP), 87
Lind, K., Asplund, M., Barklem, P. S., & Belyaev, A. K. 2011, A&A, 528, A103
Mucciarelli, A., & Bellazzini, M. 2020, RNAAS, 4, 52
Nordlander, T., & Lind, K. 2017, A&A, 607, A75
Norris, J. E., Gilmore, G., Wyse, R. F. G., Yong, D., & Frebel, A. 2010a, ApJL, 722, L104
Norris, J. E., & Yong, D. 2019, ApJ, 879, 37
Norris, J. E., Yong, D., Bessell, M. S., et al. 2013, ApJ, 762, 28
Norris, J. E., Yong, D., Gilmore, G., & Wyse, R. F. G. 2010b, ApJ, 711, 350
Placco, V. M., Frebel, A., Beers, T. C., & Stancliffe, R. J. 2014, ApJ, 797, 21
Placco, V. M., Roederer, I. U., Lee, Y. S., et al. 2021, ApJL, 912, L32
Plez, B. 2012, Turbospectrum: Code for Spectral Synthesis, Astrophysics Source Code Library, ascl:1205.004
Roederer, I. U., & Kirby, E. N. 2014, MNRAS, 440, 2665
Roederer, I. U., Preston, G. W., Thompson, I. B., et al. 2014, AJ, 147, 136
Rossi, M., Salvadori, S., & Skúladóttir, Á. 2021, MNRAS, 503, 6026
Salvadori, S., Bonifacio, P., Caffau, E., et al. 2019, MNRAS, 487, 4261
Shetrone, M. D., Côté, P., & Sargent, W. L. W. 2001, ApJ, 548, 592
Simon, J. D., Frebel, A., McWilliam, A., Kirby, E. N., & Thompson, I. B. 2010, ApJ, 716, 446
Simon, J. D., Jacobson, H. R., Frebel, A., et al. 2015, ApJ, 802, 93
Skúladóttir, Á., Andrievsky, S. M., Tolstoy, E., et al. 2015a, A&A, 580, A129
Skúladóttir, Á., Tolstoy, E., Salvadori, S., et al. 2015b, A&A, 574, A129
Skúladóttir, Á., Tolstoy, E., Salvadori, S., Hill, V., & Pettini, M. 2017, A&A, 606, A71
Starkenburg, E., Aguado, D. S., Bonifacio, P., et al. 2018, MNRAS, 481, 3838
Starkenburg, E., Hill, V., Tolstoy, E., et al. 2013, A&A, 549, A88
Suda, T., Katsuta, Y., Yamada, S., et al. 2008, PASJ, 60, 1159
Tafelmeyer, M., Jablonka, P., Hill, V., et al. 2010, A&A, 524, A58
Theler, R., Jablonka, P., Lucchesi, R., et al. 2020, A&A, 642, A176
Venn, K. A., Starkenburg, E., Malo, L., Martin, N., & Laevens, B. P. M. 2017, MNRAS, 466, 3741
Wang, E. X., Nordlander, T., Asplund, M., et al. 2021, MNRAS, 500, 2159
Yong, D., Norris, J. E., Bessell, M. S., et al. 2013, ApJ, 762, 26
Yoon, J., Beers, T. C., Dietz, S., et al. 2018, ApJ, 861, 146
Zhang, H. W., Gehren, T., & Zhao, G. 2014, in IAU Symp. 298, Setting the Scene for Gaia and LAMOST, ed. S. Feltzing et al. (Cambridge: Cambridge Univ. Press), 453